

RESEARCH ARTICLE

# Variability of seasonal precipitation extremes over China and their associations with large-scale ocean–atmosphere oscillations

Ajiao Chen<sup>1,2</sup> | Xinguang He<sup>1,3</sup>  | Huade Guan<sup>2</sup> | Xinping Zhang<sup>1,3</sup>

<sup>1</sup>College of Resources and Environmental Science, Hunan Normal University, Changsha, China

<sup>2</sup>College of Science and Engineering, Flinders University, Adelaide, South Australia, Australia

<sup>3</sup>Key Laboratory of Geospatial Big Data Mining and Application, Changsha, China

**Correspondence**

Xinguang He, College of Resources and Environmental Science, Hunan Normal University, Changsha 410081, China.  
Email: xghe@hunnu.edu.cn

**Funding information**

Construct Program of Key Discipline in Hunan Province of China, Grant/Award Number: 2011001; Hunan Bairen Program, Grant/Award Number: 2012001; National Natural Science Foundation of China, Grant/Award Numbers: 41472238 and 41571021

The spatiotemporal variations of seasonal precipitation extremes during 1963–2013 over China and the possible teleconnections with large-scale ocean–atmosphere indices are investigated by using the rotated empirical orthogonal functions, cross-correlation analysis and stepwise variable selection methods. Results show that northwest China experiences the most frequent dry events but exhibits a wetting tendency in all seasons, while in south and central China, extreme wet conditions are remarkable in seasons except for winter but a drying tendency is found in spring and autumn. Precipitation extremes in four different seasons are influenced by the different combinations of large-scale climate indices with different time lags, and their regional responses are complex when the climate indices are at different phases, such as winter heavy precipitation (R95p) in south of Nanling Mountain generally tends to be increased by the simultaneous positive El Niño–Southern Oscillation (ENSO) and sea surface temperature anomalies (SSTs) over South China Sea and positive Arctic Oscillation (AO) with 5-month lag, while summer R95p in the middle and lower reaches of Yangtze River Basin be decreased by the simultaneous negative SSTs over Bay of Bengal and positive AO with 9-month lag. Besides, the dominant climate indices identified by teleconnection analysis can partly explain the temporal changes of seasonal extreme precipitation in China, which can be confirmed by very similar fluctuation in the oscillatory patterns of eight chosen couples with higher correlation coefficient, and their explanation skill is more powerful in sensitive areas highlighted in the leading spatial modes of corresponding precipitation index. Moreover, this explanation skill generally enhances as the cumulative contribution of leading four rotated modes to total variance of the target variable over whole study area increases. In addition, the precipitation indices related to precipitation amount can be better explained than those related to wet or dry spell by identified dominant climate indices.

**KEY WORDS**

China, empirical orthogonal functions, seasonal precipitation extremes, stepwise variable selection, teleconnection

## 1 | INTRODUCTION

Occurrence of extreme climate events has received increasing attention due to its large negative impacts on human societies, and the patterns of occurrence may change with global climate change. The IPCC (Intergovernmental Panel

on Climate Change) reports (IPCC, 2012) suggest that occurrence of extreme events is very likely to change in intensity, frequency and location in the 21st century. An enormous progress has been made in quest of an improved understanding of extreme events, with an aim to produce predictive products to help manage and prevent the

associated risks. However, we are still facing multiple challenges, such as limitations in understanding the processes of extreme events and building models for predicting future extremes (Zwiers *et al.*, 2013).

China is vulnerable to climate extremes because of ageing, high density and mobility of population, rapid accumulation of social wealth and poor infrastructure for disaster prevention and mitigation. In addition, Qin *et al.* (2015) reported that in the 21st century, meteorological disasters in China resulting from climate extremes led to an annual economic loss equivalent to 1.07% of the gross domestic product (GDP), which was much higher than the global average loss (0.14%). Therefore, any changes in climate extremes over China are of particular concern. Several studies reported that annual extreme precipitation has increased in northwest China (Zhang *et al.*, 2012; Jiang *et al.*, 2013), the middle and lower reaches of the Yangtze River basin, parts of the southwest and south China coastal areas (Zhai *et al.*, 2005), and decreased in north China (Fan *et al.*, 2012), Yellow River basin (Fu *et al.*, 2013) and the Sichuan Basin (Zhai *et al.*, 2005). Increasing trends of extreme precipitation have been observed in all seasons in northwest China, but in the Yangtze River basin, extreme precipitation only increased in winter and summer (Wang and Yang, 2017). Thus, seasonal features are important for gaining more detailed information of changes in extreme precipitation. There exist some studies on the variability of extreme precipitation in China and their associations with different influencing factors (Fu *et al.*, 2013; Yang *et al.*, 2013; Wang *et al.*, 2014; Gu *et al.*, 2017; Wang and Yang, 2017; Xiao *et al.*, 2017). However, the studies on both wet and dry climate extremes at seasonal scale over the whole China remain rare.

Climate varies in China due to its large geographical size and complex topographic relief, with a range from the arid desert in the northwest to the humid coastal area in the southeast. Precipitation over China is influenced by complex interactions of ocean, atmosphere and land surface processes (Peng *et al.*, 2014). Relationships between extreme precipitation and large-scale ocean–atmosphere indices can be useful for predicting the occurrence of extreme events (Paredes Trejo *et al.*, 2016; Sillmann *et al.*, 2017). El Niño–Southern Oscillation (ENSO) represented by NINO3 and NINO3.4 is a coupled ocean–atmosphere tropical Pacific phenomenon with global influence. The influences of ENSO events on precipitation regimes have been investigated widely (e.g., Gershunov and Barnett, 1998; Grimm and Tedeschi, 2009), including in China (e.g., Peng *et al.*, 2014; Xiao *et al.*, 2015). The climate of eastern China is dominated by the East Asian monsoon which is significantly influenced by ENSO. Pacific Decadal Oscillation (PDO) and the Indian Ocean Dipole mode index (DMI) also have a certain impact on the East Asian monsoon (Yuan *et al.*, 2008; Chen *et al.*, 2013). Besides, sea surface temperature anomalies (SSTs)

over other regions, such as South China Sea (SCS), East China Sea (ECS) and Bay of Bengal (BB), have been reported with connections to precipitation over China (Peng *et al.*, 2014). The Arctic Oscillation (AO) and the North Atlantic Oscillation (NAO) have also been found to influence precipitation over China both individually and in conjunction with other SSTs (Gong and Ho, 2003; Linderholm *et al.*, 2011).

These relationships are often investigated by linear correlation or regression analyses (e.g., Yang *et al.*, 2013; Wang *et al.*, 2014; Wang and Yang, 2017). The chaotic nature of meteorological processes and large precipitation spatial variabilities make direct analyses between precipitation at a certain area and selected large-scale ocean–atmosphere climate indices difficult. The empirical orthogonal functions (EOFs) are useful to identify coherent patterns of spatial and temporal variability of the variables, which is widely applied in meteorological studies (e.g., Casanueva Vicente *et al.*, 2014; Zilli *et al.*, 2016; Ying *et al.*, 2018). In addition, the rotation of a certain number of modes is carried out for identifying intrinsic modes of climate variability in particular regions. Grimm and Saboia (2015) used the rotated empirical orthogonal functions (REOFs) to reveal the inter-decadal variability modes of monsoon precipitation over South America and their connections with large-scale climate indices. Xiao *et al.* (2015) applied REOFs to analyse the teleconnections between ENSO, NAO, Indian Ocean Dipole (IOD), PDO and seasonal precipitation regimes over the Yangtze River basin, China. These studies have proved that the precipitation regimes can be well illustrated by the REOFs method. In addition, the temporal patterns of the leading rotated modes can provide possibility for further investigation into finding out the drivers of precipitation change.

The objectives of this study are (a) to examine the spatial distribution and trends of seasonal precipitation extremes during 1963–2013 over China, (b) to investigate coherent spatial patterns of temporal variability of seasonal precipitation extremes and (c) to identify the dominant climate factors in explaining extreme precipitation changes by analysing the statistical association between temporal patterns of precipitation extremes with large-scale ocean–atmosphere indices. The results of this study will provide insight into regional response of precipitation extremes in China to global climate indices, and contribute to the seasonal climate extreme forecast and disaster prevention.

## 2 | DATA

### 2.1 | Precipitation data

The daily precipitation data of 3,825 grid points ( $0.5 \times 0.5^\circ$ ) during 1963–2013 were downloaded from the China Meteorological Data Sharing Service Network

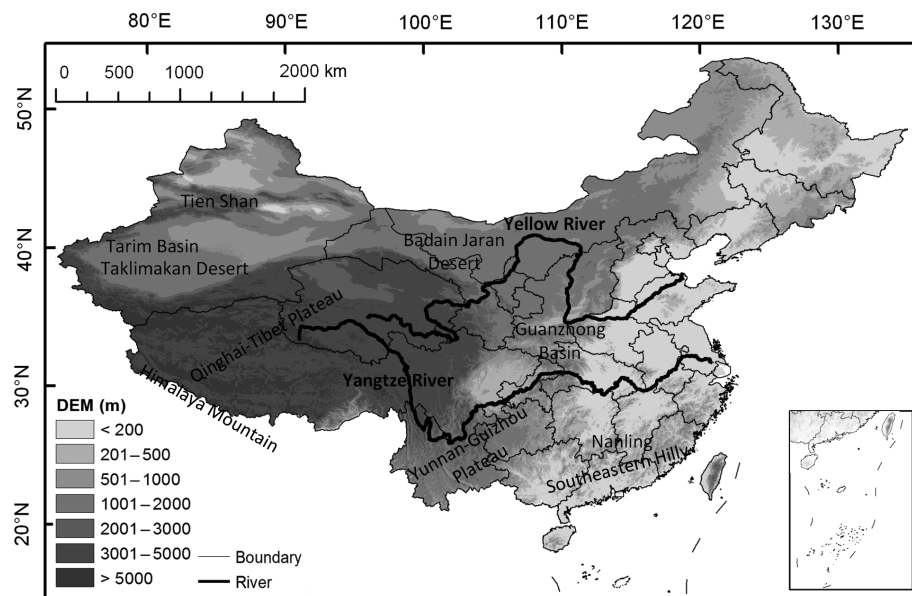


**FIGURE 1** Topography of China and locations of important terrain areas involved in this study

(<http://data.cma.cn/>), which were obtained by interpolation of observed data from 2,472 stations over China. It is necessary to note that the quality of observed data have been controlled and the digital elevation data have been introduced in order to eliminate the impacts of terrain on precision of spatial interpolation. The topography of China and locations of important terrain areas are shown in Figure 1.

## 2.2 | Climate indices

A number of large-scale ocean–atmosphere indices have been identified to have teleconnections with the variability of precipitation in China. The SST is an important influencing factor of climate change. In this study, NINO3 and NINO3.4 are selected to represent SSTs in the tropical central and eastern Pacific Ocean dominated by ENSO. Other SSTs related indices including SCS, ECS, BB, DMI and PDO are also selected in order to investigate their linkages with extreme precipitation over China. In addition, large-scale atmospheric circulation variables, AO and NAO have

been used for rainfall prediction in China (see, e.g., Hartmann *et al.*, 2008; Peng *et al.*, 2014). They are chosen for this study too. Table 1 gives a brief description of the nine selected climate indices.

## 3 | METHODS

### 3.1 | Extreme indices

A suite of 27 extreme indices have been defined by the Expert Team on Climate Change Detection and Indices (ETCCDI) in order to reveal the changing characteristics of climate extremes, which provide a comprehensive overview of temperature and precipitation statistics (Peterson *et al.*, 2001; Peterson, 2005). Following Casanueva Vicente *et al.* (2014), three seasonal extreme precipitation indices (Table 2) are chosen because they are useful to present both dry (consecutive dry days (CDD)) and wet (consecutive wet days (CWD), heavy precipitation (R95p)) conditions. The CWD and CDD,

**TABLE 1** List of the selected large-scale ocean–atmosphere indices

Climate indices	Definitions	Source
NAO (North Atlantic Oscillation)	The normalized pressure difference between a station on the Azores and one on Iceland	<a href="http://www.cpc.ncep.noaa.gov">http://www.cpc.ncep.noaa.gov</a>
AO (Arctic Oscillation)	The first leading EOF mode of monthly mean height anomalies at 1,000 hPa	<a href="http://www.cpc.ncep.noaa.gov">http://www.cpc.ncep.noaa.gov</a>
NINO3 (Niño3 SST index)	Average SST anomaly over 150°–120°W, 5°N–5°S	<a href="http://www.cpc.ncep.noaa.gov">http://www.cpc.ncep.noaa.gov</a>
NINO3.4 (Niño 3.4 SST index)	Average SST anomaly over 170°–120°W, 5°N–5°S	<a href="http://www.cpc.ncep.noaa.gov">http://www.cpc.ncep.noaa.gov</a>
PDO	Leading principal component of monthly SST anomalies in the North Pacific Ocean, polewards of 20°N	<a href="http://www.esrl.noaa.gov">http://www.esrl.noaa.gov</a>
DMI	Difference between SST anomaly over 50°–70°E, 10°N–10°S and 90°–110°E, 0°–10°S	<a href="http://www.cdc.noaa.gov">http://www.cdc.noaa.gov</a>
SCS (SSTs over South China Sea)	Average SST anomaly over 100°–120°E, 0°–25°N	<a href="http://www.cdc.noaa.gov">http://www.cdc.noaa.gov</a>
ECS (SSTs over East China Sea)	Average SST anomaly over 118°–128°E, 23°–33°N	<a href="http://www.cdc.noaa.gov">http://www.cdc.noaa.gov</a>
BB (SSTs over Bay of Bengal)	Average SST anomaly over 87°–89°E, 7°–23°N and 80°–96°E, 14°–16°N	<a href="http://www.cdc.noaa.gov">http://www.cdc.noaa.gov</a>

**TABLE 2** Definition of the extreme precipitation indices used in this study ([http://etcddi.pacificclimate.org/indices\\_def.shtml](http://etcddi.pacificclimate.org/indices_def.shtml))

ID	Indicator name	Definitions	Units
R95p	Heavy precipitation	Total precipitation from days >95th percentile	mm
CWD	Consecutive wet days	Maximum number of consecutive days with precipitation $\geq 1$ mm	Days
CDD	Consecutive dry days	Maximum number of consecutive days with precipitation $< 1$ mm	Days

respectively, represent the maximum consecutive wet and dry days in prescribed time intervals. They are both related to the precipitation occurrence, which characterize wetness and droughts indirectly. In addition, R95p determines the intensity of very heavy precipitation events, which exams the contribution of the top 5% extreme precipitation days to the total precipitation.

### 3.2 | Trend analysis

The simple linear regression method and the Mann–Kendall (M–K) test (Mann, 1945; Kendall, 1975) are used in this study to detect the trends of seasonal precipitation indices. We choose a significance level of 5% for the M–K test. The linear regression method and the M–K test have been widely used to assess the trend and significance of the hydro-meteorological time series by many researchers (e.g., Gemmer *et al.*, 2011; Wang *et al.*, 2013; Chen *et al.*, 2018).

### 3.3 | Rotated EOFs

The EOFs have been wildly used in meteorological studies. The decomposition of a continuous space–time field, where and denote, respectively, time and spatial position, can be described as (Hannachi *et al.*, 2007),

$$X(t, s) = \sum_{k=1}^K c_k(t) u_k(s), \quad (1)$$

where  $K$  is the number of modes contained in the field,  $u_k(s)$  are orthogonal spatial functions and  $c_k(t)$  are corresponding temporal patterns. For convenience, in this paper we use the terminology EOFs and principal components (PCs) for the spatial and temporal patterns, respectively. In general, the spatial orthogonality and temporal non-correlation of EOFs and PCs, respectively, impose limits on physical interpretability of EOF patterns as physical processes are not necessarily independent. A rotation of EOFs can systematically alter the structures of EOFs (Hannachi *et al.*, 2007) which may help to address the problem.

In this study, the EOFs and REOFs methods introduced in Hannachi *et al.* (2007) are followed. The EOFs are used to decompose space–time field of the seasonal precipitation indices into the spatial patterns and associated temporal

patterns, and then the modes which pass the 5% significance test (North *et al.*, 1982) are rotated by VARIMAX algorithm to present the seasonal extreme precipitation regimes. The VARIMAX is the most well-known and commonly used rotation algorithm. Given a  $p \times m$  matrix  $U_m = (u_1, u_2, \dots, u_m)$  of the leading  $m$  EOFs, the rotation is achieved by finding out an  $m \times m$  rotation matrix  $R$  to construct the rotated EOFs matrix  $B$ , according to

$$B = U_m R. \quad (2)$$

Let  $b_{ij}$  ( $i = 1, \dots, p$  and  $j = 1, \dots, m$ ) denote the elements of the rotated EOFs matrix  $B$  in Equation (2). Then, the VARIMAX orthogonal rotation maximizes a simplicity criterion according to

$$\max \left( f(B) = \sum_{k=1}^m \left[ p \sum_{j=1}^p b_{jk}^4 - \left( \sum_{j=1}^p b_{jk}^2 \right)^2 \right] \right), \quad (3)$$

where  $m$  is the number of EOFs chosen for rotation. In some cases, to reduce the bias towards the first EOF with the largest eigenvalue, the loadings of the rotated  $B$  are weighted by the communalities of different variables. The communalities  $h_j^2$  ( $j = 1, \dots, p$ ) are directly proportional to the sum of squares  $\sum_{k=1}^m u_{jk}^2$  of the loadings for a particular variable. Hence if  $C = \text{Diag}(U_m U_m^T)^{-1/2}$ , then in the weighted or normalized VARIMAX, the matrix  $B$  in Equation (3) is simply replaced by  $BC$ .

### 3.4 | Multiple linear regression

Multiple linear regression (MLR) with stepwise variable selection can be used to determine the relative importance of different predictor variables in explaining the predictand variable (Clow, 2010). In this study, the lag cross-correlation analysis is first conducted to examine the lag relationship between the temporal pattern of extreme precipitation indices and the climate indices with time lags of 0–12 months. Then, the climate indices significantly related to extreme precipitation indices are identified as the potential predictor variables for estimating temporal variability of precipitation extremes. Here, the MLR is written as,

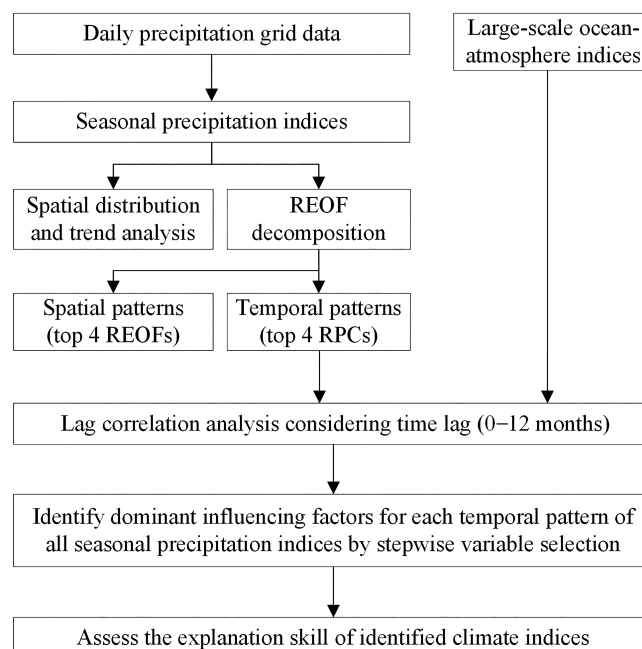
$$\hat{y}(t_n) = a_0 + a_1 x_1(t_{n-\tau_1}) + a_2 x_2(t_{n-\tau_2}) + \dots + a_i x_i(t_{n-\tau_i}) + \dots, \quad (4)$$

where  $\hat{y}(t_n)$  is the rotated PC (RPC) of seasonal precipitation index,  $x_i$  ( $i = 1, \dots, I$ ) is the  $i$ th potential large-scale ocean–atmosphere index,  $\tau_i$  is the lag time between the RPC and the  $i$ th climate index (positive lag indicates climate index leading) and  $a_i$  is the model regression parameter. In this study, a stepwise variable selection method (Draper and Smith, 1998) is applied to prevent overfitting the data and select significant climate indices from all potential predictor variables. The stepwise regression is a systematic method for adding terms to and removing terms from a multiple linear model based on

their statistical significance in a regression. The statistical significance of the regression model is assessed by means of *F*-test. The final chosen climate indices are considered as the dominant driving factors for the corresponding precipitation temporal pattern, and their contribution percentage to the temporal change of precipitation modes can also be estimated through the coefficient of determination ( $R^2$ ) of the MLR.

### 3.5 | Data analysis flow chart

The outline of the steps involved in this study is shown in Figure 2. First, the spatial distributions and trends of seasonal precipitation extremes are analysed based on extreme precipitation indices derived from daily precipitation grid data. Here, the trend tests are completed by using the simple linear regression method and the M-K test. Then, the REOFs method is applied to reveal the spatial patterns of each seasonal precipitation index, and the cross-correlation analysis and stepwise variable selection are used to identify the dominant influencing factors from several candidate climate indices with time lags of 0–12 months. The identified climate indices are used to reveal how much variability (indicated by coefficient of determination  $R^2$ ) of temporal pattern of corresponding REOFs can be explained. Finally, in order to assess the explanation skill of identified climate indices, we calculate the regression  $R^2$  for all corresponding undecomposed seasonal precipitation indices in each of grid cells. In addition, the correlation between cumulative explained variance by the first four rotated modes versus the areal mean and maximum regression  $R^2$  in the whole study area is also examined.



## 4 | RESULTS

### 4.1 | Spatial distribution of seasonal precipitation extreme indices

The accumulated precipitation (PPT) is included to compare with the three extreme indicators (R95p, CWD and CDD). The spatial distributions of average seasonal PPT, R95p, CWD and CDD during 1963–2013 over China are shown in Figure 3. Obvious spatial differences can be observed, which tells that south and central China are wetter while northwest China is driest in all seasons. In winter, heavy precipitation seldom occurs while extreme dry events are remarkable in China (Figure 3a–d). In this season, extreme wet condition R95p is generally less than 20 mm in China except for coastal areas in southeast China (Figure 3b). Driest condition of winter is observed in the northwestern areas of China, especially in Qinghai–Tibet Plateau, Tarim Basin and Inner Mongolia, where the highest CDD is up to more than 60 days (Figure 3d). In spring (Figure 3e–h), the southern and central areas of China are wetter while northwest China is drier but not as serious as winter. Summer (Figure 3i–l) has the largest precipitation amount among all seasons over a large portion of the study area. In autumn (Figure 3m–p), wetter areas are located in south and central China, and dry condition is also most visible in northwest China. Except for some areas located in northern Sinkiang, CDD exceeds 30 days in northwest China, and is up to over 60 days in its dry centre (Figure 3p).

### 4.2 | Trends of seasonal precipitation indices

The maps of trends for PPT and three extreme precipitation indices R95p, CWD and CDD are shown in Figure 4 for each season. We can see from the first column of Figure 4 that winter precipitation was increasing in most areas during the past decades. In the northwest corner of China (north of Tien Shan) three wet indices show significant increasing trends (Figure 4a–c), while the dry index CDD exhibits a significant decreasing trend (Figure 4d). Significant increasing trends of winter PPT and CWD are also observed in the northeastern area of China. Sparse grids with significant decreasing trends of three wet indices are mainly distributed in the southeastern corner of Tibet. Winter CDD shows decreasing trends in most areas and significantly decreases in the northwest China, Qinghai–Tibet region, and northeastern area of China. Significant increase in the number of consecutive dry days is found in the southeastern corner of Tibet, which is consistent with the change of the wet indices in this area. In spring, significant increasing PPT (Figure 4e) and R95p (Figure 4f) are mainly observed in the Qinghai–Tibet region where the dry index CDD (Figure 4h) exhibits a significant decreasing trend. Besides, spring CDD also shows a significant decreasing trend in northeast China. Significant decreasing trends of spring CWD (Figure 4g) are

FIGURE 2 Outline of the steps involved in this study

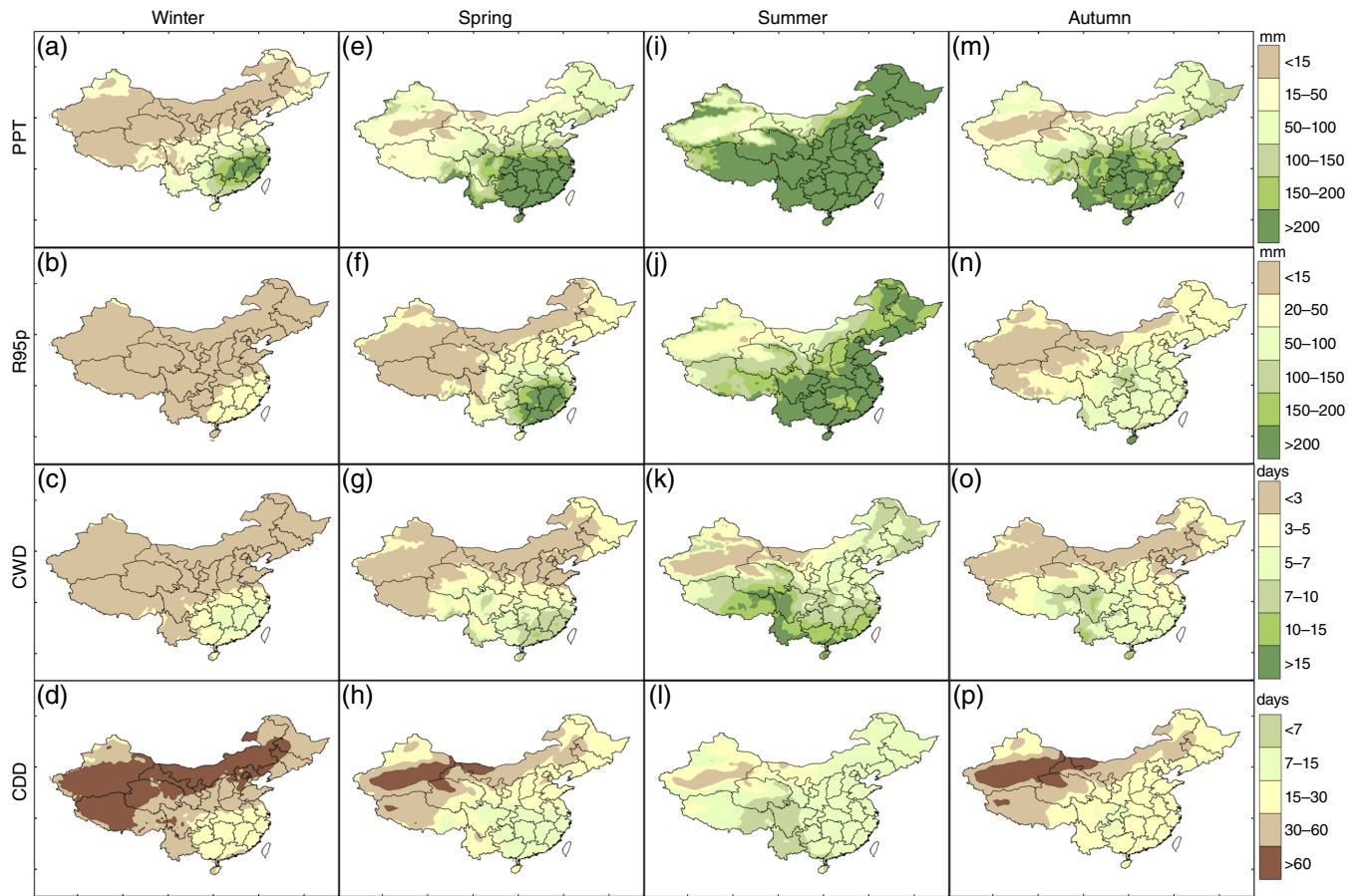


**FIGURE 3** Spatial distribution of multiyear mean seasonal precipitation indices PPT, R95p, CWD and CDD

scattered in south China while grids with significant increasing trends are mainly concentrated in the central area of Tibet. As for summer, significant increasing PPT (Figure 4i) and R95p (Figure 4j) are mostly observed in Qinghai–Tibet region. Significant decreasing CDD (Figure 4l) is concentrated in northwest China. Autumn precipitation has increased in northwest China while decreasing in northeast and south China. Most obvious decreasing trends of CWD are observed in autumn with most significant grids concentrated in south, central and northeast China (Figure 4o). Autumn CDD increases significantly in the southern area of China (Figure 4p). Over all the seasons, in terms of the spatial variability of temporal trends, results of wet indices are generally coincident with those of the dry index CDD. PPT shows largest magnitude of trends than three extreme indices. In addition, the extreme index related to precipitation amount shows larger magnitude of trends than those related to wet or dry spell.

#### 4.3 | Spatial patterns of seasonal precipitation indices and associations with climate indices

The space–time fields of seasonal precipitation indices have been decomposed by the EOFs and then those modes passed the 5% significance test have been rotated by VARIMAX

algorithm. We select the first four modes of rotated EOFs to present the seasonal precipitation regimes, and the explained variances of the leading four REOFs for each season are listed in Table 3. The spatial patterns of the leading four rotated EOFs for precipitation indices can illustrate the main features of those indices for each season, and the sensitive areas (high/low-value centre) can be highlighted by those rotated modes. Then, the simultaneous and lag (in month) correlations between the large-scale ocean–atmosphere indices and the temporal patterns of the first four rotated EOFs are calculated. The stepwise regression method is used to reveal how much variability of temporal pattern of REOFs can be explained by the sum of the dominant climate indices, which is evaluated by the coefficient of determination  $R^2$ . We note that the temporal patterns of REOFs have been detrended in case that the results of correlation analysis might be influenced by trends. The spatial patterns of precipitation indices and their associations with climate indices are presented in the following sections for each of four seasons: winter, spring, summer and autumn.

##### 4.3.1 | Winter

For winter precipitation indices, the spatial patterns of the leading four rotated EOFs are shown in Figure 5, and the dominant influencing factors identified by stepwise

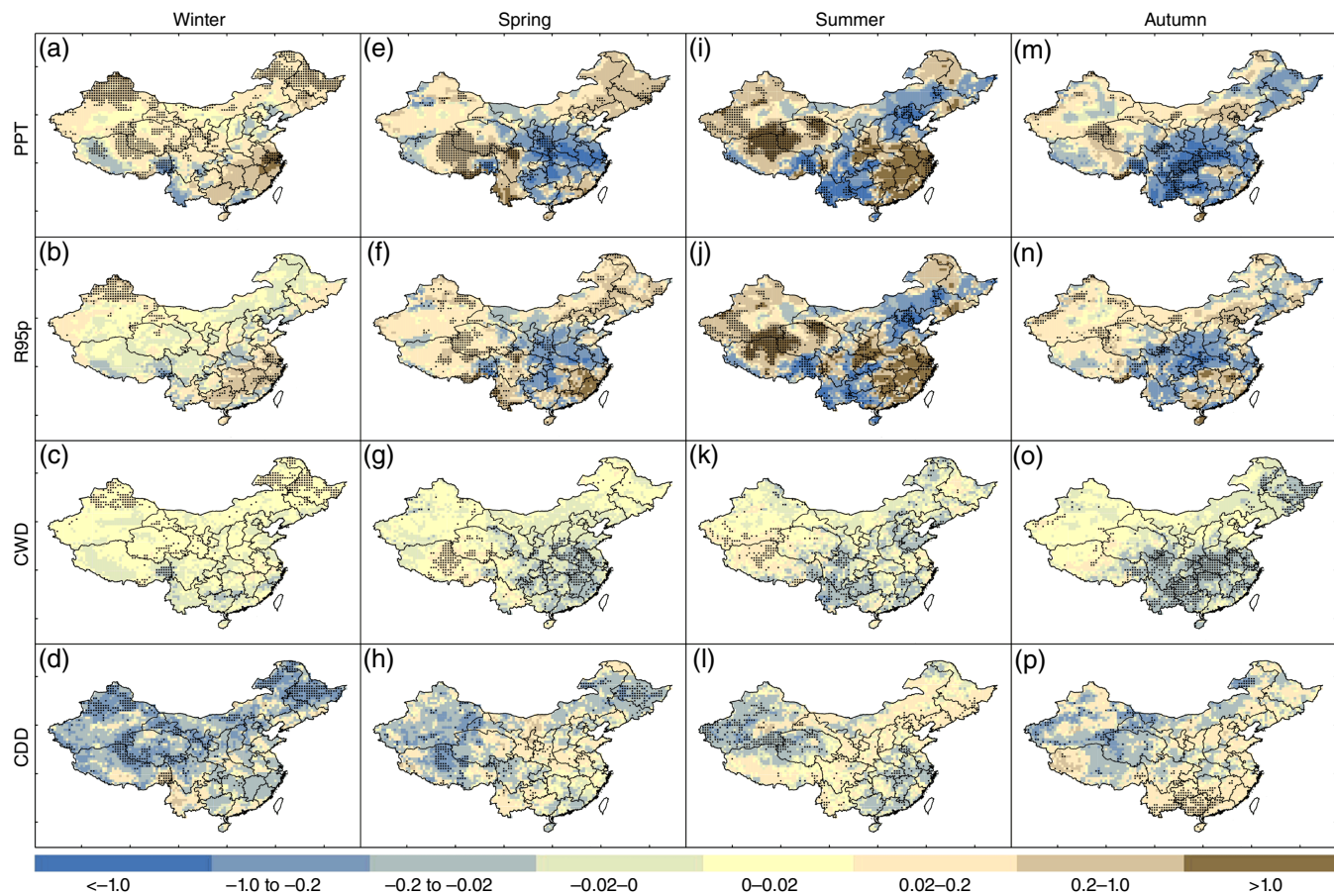


**FIGURE 4** Trend maps of PPT, R95p, CWD and CDD in four different seasons. Yellow (blue) means upwards (downwards) trends. The black dots correspond to those points whose trends are statistically significant at 5% significance level

**TABLE 3** Explained variances of the leading four REOFs for each season

Indices	REOF1 (%)	REOF2 (%)	REOF3 (%)	REOF4 (%)	Cumulative (%)
winter_PPT	46.06	15.54	8.45	7.41	77.46
winter_R95p	36.32	13.34	6.06	4.70	60.42
winter_CWD	12.54	10.52	5.57	4.77	33.40
winter_CDD	14.13	7.42	6.25	4.56	32.36
spring_PPT	33.45	18.18	5.70	5.54	62.87
spring_R95p	27.61	12.59	5.89	4.82	50.91
spring_CWD	13.76	9.13	5.70	4.18	32.77
spring_CDD	8.31	7.03	6.17	5.76	27.27
summer_PPT	18.49	12.64	8.08	5.88	45.09
summer_R95p	15.13	9.47	6.14	5.57	36.31
summer_CWD	13.05	10.02	5.08	4.16	32.31
summer_CDD	16.74	6.43	5.14	4.50	32.81
autumn_PPT	20.77	15.25	5.52	4.78	46.32
autumn_R95p	13.47	10.76	6.65	5.53	36.41
autumn_CWD	15.90	7.18	6.12	5.21	34.41
autumn_CDD	12.61	11.74	6.91	5.21	36.47

regression for the first four rotated modes of winter precipitation indices and their coefficient of determination  $R^2$  for explaining the temporal variability of the corresponding RPCs are shown in Table 4. It can be seen from Table 4 that the NINO3 index is an important influencing factor for winter precipitation, which shows the most significant impacts

on the first rotated modes for winter PPT, R95p and CDD. Positive NINO3\_10 and negative NAO\_7 tend to increase winter CDD in the northern area of Henan Province located in central China (Figure 5d), and 21% temporal variation in RPC1 for winter CDD can be explained by these two climate indices. To the south of Nanling Mountain which is a known

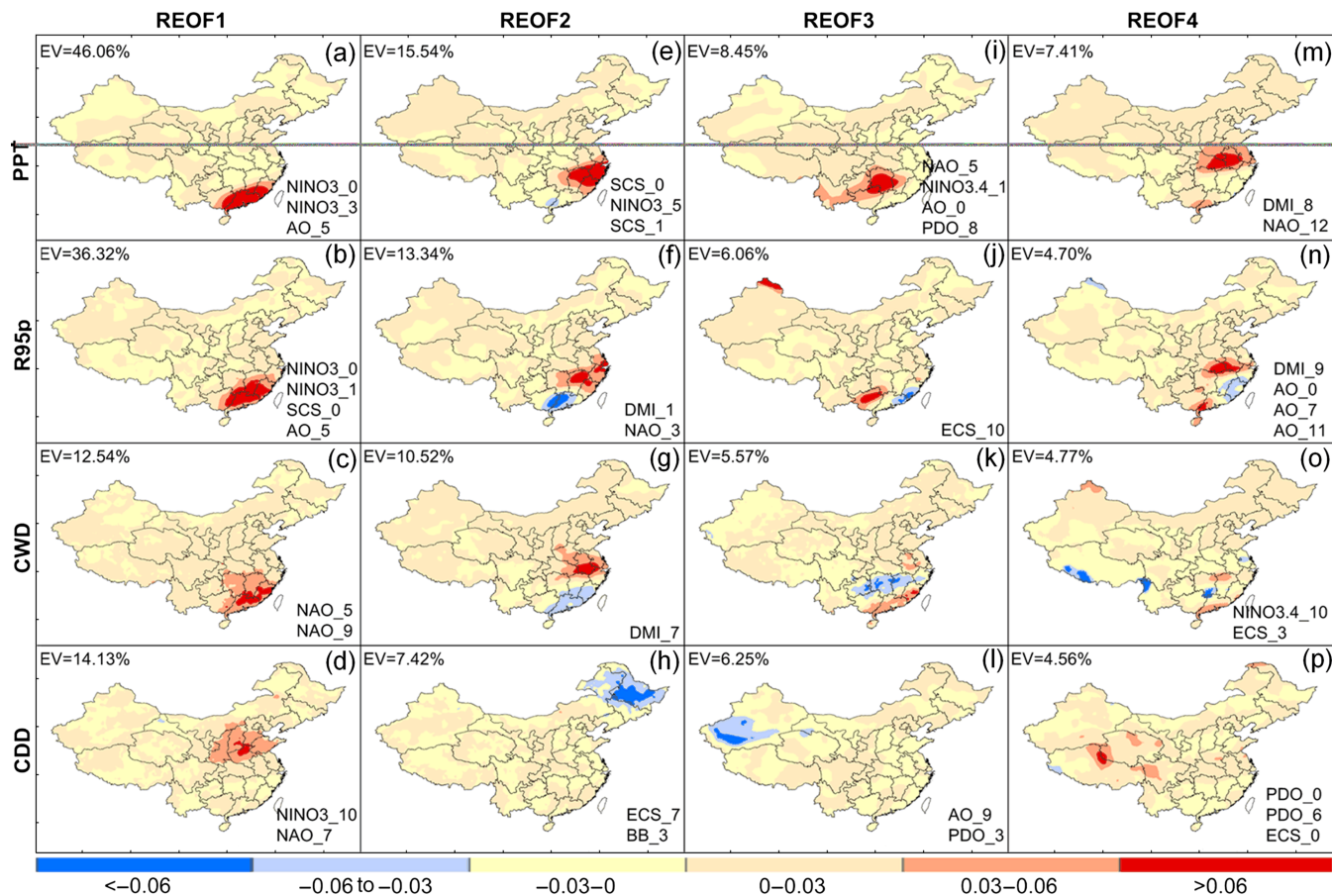


**FIGURE 5** Spatial patterns of the leading four rotated EOFs for winter precipitation indices. EV represents the explained variance by corresponding mode. The climate indices shown in the lower right corner of each subgraph are the corresponding dominant influencing factors identified by the stepwise regression, where the suffix of climate indices denotes time lag

**TABLE 4** Dominant influencing factors identified by stepwise regression for the leading four rotated modes of winter precipitation indices and their cumulative contribution percentage (as shown by the coefficient of determination  $R^2$ ) to the corresponding RPCs

RPCs	Dominant influencing factors			$R^2$	
PPT_RPC1	NINO3_0 (0.43)	NINO3_3 (0.29)	AO_5 (0.28)	44.10	
PPT_RPC2	SCS_0 (0.54)	NINO3_5 (0.43)	SCS_1 (0.42)	41.04	
PPT_RPC3	NAO_5 (0.41)	NINO3.4_1 (0.37)	AO_0 (0.35)	PDO_8 (0.29)	49.30
PPT_RPC4	DMI_8 (-0.37)	NAO_12 (0.32)			27.34
R95p_RPC1	NINO3_0 (0.50)	NINO3_1 (0.44)	SCS_0 (0.33)	AO_5 (0.31)	58.48
R95p_RPC2	DMI_1 (0.37)	NAO_3 (-0.32)			24.70
R95p_RPC3	ECS_10 (0.37)				13.33
R95p_RPC4	DMI_9 (-0.52)	AO_0 (0.44)	AO_7 (0.40)	AO_11 (0.39)	54.31
CWD_RPC1	NAO_5 (0.42)	NAO_9 (0.31)			24.30
CWD_RPC2	DMI_7 (-0.41)				16.42
CWD_RPC4	NINO3.4_10 (-0.40)	ECS_3 (0.31)			26.10
CDD_RPC1	NINO3_10 (0.37)	NAO_7 (-0.29)			21.26
CDD_RPC2	ECS_7 (0.37)	BB_3 (0.37)			22.06
CDD_RPC3	AO_9 (0.37)	PDO_3 (-0.32)			21.90
CDD_RPC4	PDO_0 (-0.47)	PDO_6 (-0.32)	ECS_0 (-0.31)		37.49

Note. All correlation coefficients in the brackets are statistically significant at the 5% significance level, and the suffix of climate indices denotes time lag (0–12 months).

demarcation line of precipitation in China, positive NINO3\_0, NINO3\_3 and AO\_5 tend to increase winter PPT (Figure 5a) while positive NINO3\_0, NINO3\_1, SCS\_0 and AO\_5 tend to increase winter R95p there (Figure 5b). In

addition, temporal changes in the first rotated modes for winter PPT and R95p in that area can be, respectively, explained 44 and 58% by their corresponding dominant influencing factors. The sensitive area of the first rotated

mode for winter CWD (Figure 5c) is also located in south of Nanling Mountain, but its most significant influencing factor is NAO. NAO\_5 and NAO\_9 together are shown to explain 24% temporal changes in RPC1 of winter CWD. The explained variances of the first four rotated modes are in descending order, but the dominant influencing factors identified by the second, third, and fourth modes might also be potential predictors for precipitation changes. So in section 4.4, the dominant climate indices identified by the first four rotated modes of each season precipitation index will be used as input variables for the corresponding MLR analysis to assess their explanation skill.

#### 4.3.2 | Spring

In spring (see Figure 6 and Table 5), south China area enters the rainy season. The sensitive areas of the first rotated modes of spring PPT, R95p and CWD are all located in the southeastern part of Southeastern Hilly area (Figure 6a–c). Table 5 indicates that the SCS shows the most significant impacts on the first rotated modes of both spring PPT and R95p. Positive SCS\_0 and negative AO\_0, DMI\_2, ECS\_8 tend to increase spring PPT in the southeastern part of Southeastern Hilly area (Figure 6a), and these four factors together are reported to explain 43% temporal changes in RPC1 of spring PPT. SCS\_0, PDO\_0 and DMI\_11 together are reported to explain 38% temporal changes in RPC1 of

spring R95p. The number of spring consecutive wet days in the southeastern part of Southeastern Hilly area tends to be increased by negative ECS\_8, DMI\_10 and positive DMI\_2 (Figure 6c), and those three factors together explain 35% temporal variation in RPC1 of spring CWD. As for dry condition of spring, positive DMI\_11 and negative AO\_0 tend to increase spring CDD in Badain Jaran Desert (Figure 6d), and 24% temporal changes in RPC1 of spring CDD can be explained by these two climate indices. The sensitive areas of the second rotated modes of three wet precipitation indices are all located in the middle and lower regions of the Yangtze River Basin excluding coastal areas (Figure 6e–g). NINO3\_9 and PDO\_12 together can explain 21% variability in RPC2 for spring PPT, BB\_4 and PDO\_12 together explain 21% variability in RPC2 for spring R95p, and NINO3.4\_1 and DMI\_0 together are reported to explain 26% variability in RPC2 for spring CWD. Positive NINO3.4\_12, BB\_0 and negative DMI\_10 tend to decrease spring CDD in the western part of Taklimakan Desert (Figure 6h), and 33% temporal changes in RPC2 of spring CDD can be explained by these climate indices.

#### 4.3.3 | Summer

In summer (see Figure 7 and Table 6), the sensitive areas of REOF1 for PPT (Figure 7a) and R95p (Figure 7b) are both located in the middle and lower regions of Yangtze River

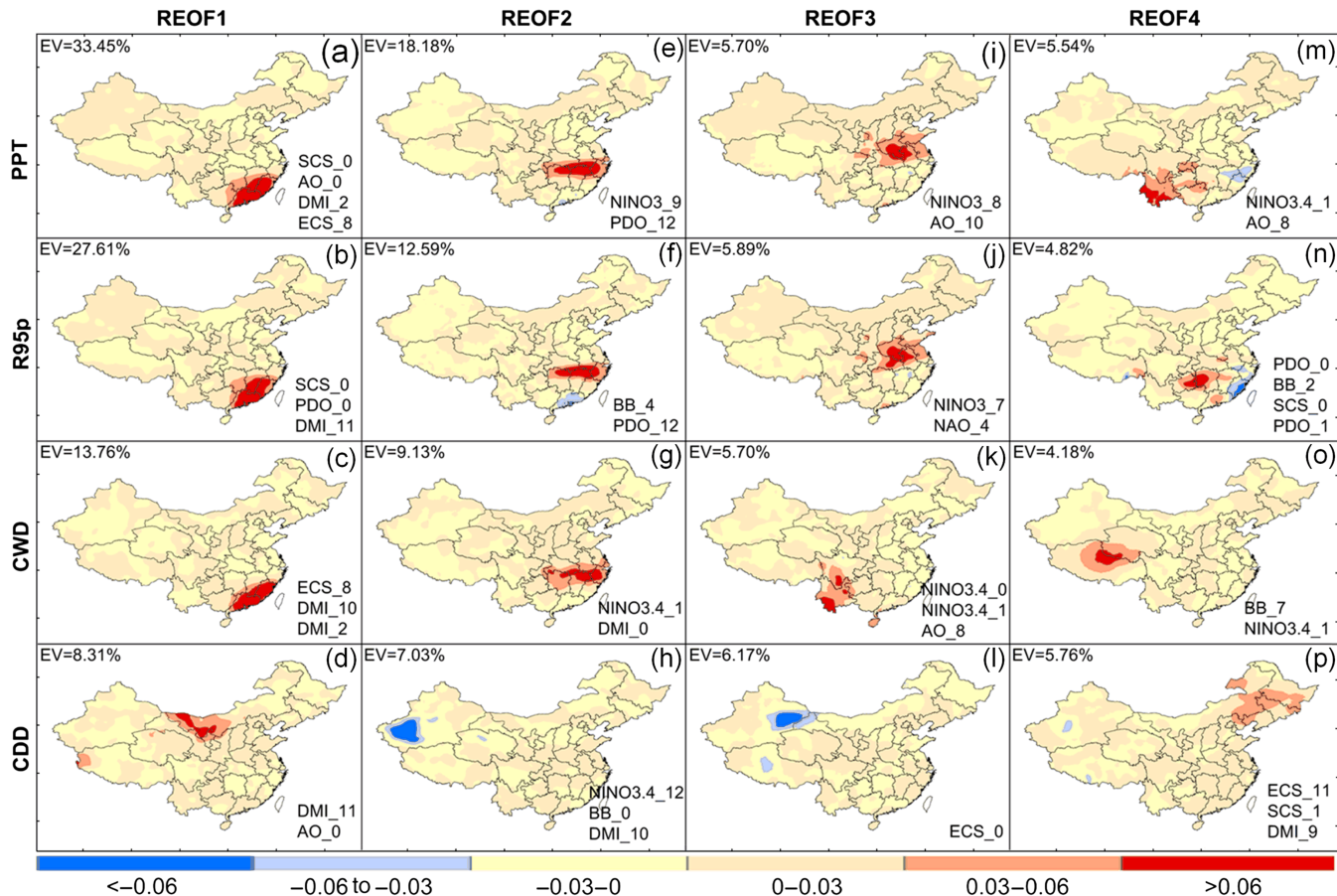


FIGURE 6 Spatial patterns of the leading four rotated EOFs for spring precipitation indices

TABLE 5 As Table 4, but for spring

RPCs	Dominant influencing factors				$R^2$
PPT_RPC1	SCS_0 (0.40)	AO_0 (-0.39)	DMI_2 (-0.35)	ECS_8 (-0.33)	43.24
PPT_RPC2	NINO3_9 (0.34)	PDO_12 (-0.31)			21.43
PPT_RPC3	NINO3_8 (0.48)	AO_10 (-0.35)			32.32
PPT_RPC4	NINO3.4_1 (-0.45)	AO_8 (0.41)			31.75
R95p_RPC1	SCS_0 (0.44)	PDO_0 (0.31)	DMI_11 (0.30)		38.43
R95p_RPC2	BB_4 (0.37)	PDO_12 (-0.28)			21.48
R95p_RPC3	NINO3_7 (0.49)	NAO_4 (-0.30)			32.50
R95p_RPC4	PDO_0 (-0.35)	BB_2 (-0.34)	SCS_0 (-0.28)	PDO_1 (-0.28)	45.17
CWD_RPC1	ECS_8 (-0.44)	DMI_10 (0.34)	DMI_2 (-0.32)		34.52
CWD_RPC2	NINO3.4_1 (0.39)	DMI_0 (-0.39)			25.59
CWD_RPC3	NINO3.4_0 (-0.48)	NINO3.4_1 (-0.37)	AO_8 (0.32)		40.33
CWD_RPC4	BB_7 (0.47)	NINO3.4_11 (-0.35)			46.91
CDD_RPC1	DMI_11 (0.41)	AO_0 (-0.32)			23.60
CDD_RPC2	NINO3.4_12 (0.40)	BB_0 (0.34)	DMI_10 (-0.32)		32.66
CDD_RPC3	ECS_0 (0.50)				25.19
CDD_RPC4	ECS_11 (-0.39)	SCS_1 (-0.36)	DMI_9 (-0.30)		31.87

basin excluding coastal areas, where the summer accumulated precipitation and heavy precipitation both tend to be increased by positive BB\_0 together with negative AO\_9. These two climate indices together are reported to explain 24 and 23% temporal changes in RPC1 of summer PPT and R95p, respectively. It can be seen from REOF1 of summer CWD (Figure 7c) that the negative SCS\_4 and positive

DMI\_6 tend to increase summer consecutive wet days in the southwestern area of Yunnan Province, and these two factors together can explain 25% temporal changes in RPC1 of summer CWD. As for dry condition, negative ECS\_4 tends to increase summer CDD in Tarim Basin area (Figure 7d). ECS\_4 is the unique influencing factor that is reported to explain 19% temporal changes in RPC1 of summer CDD.

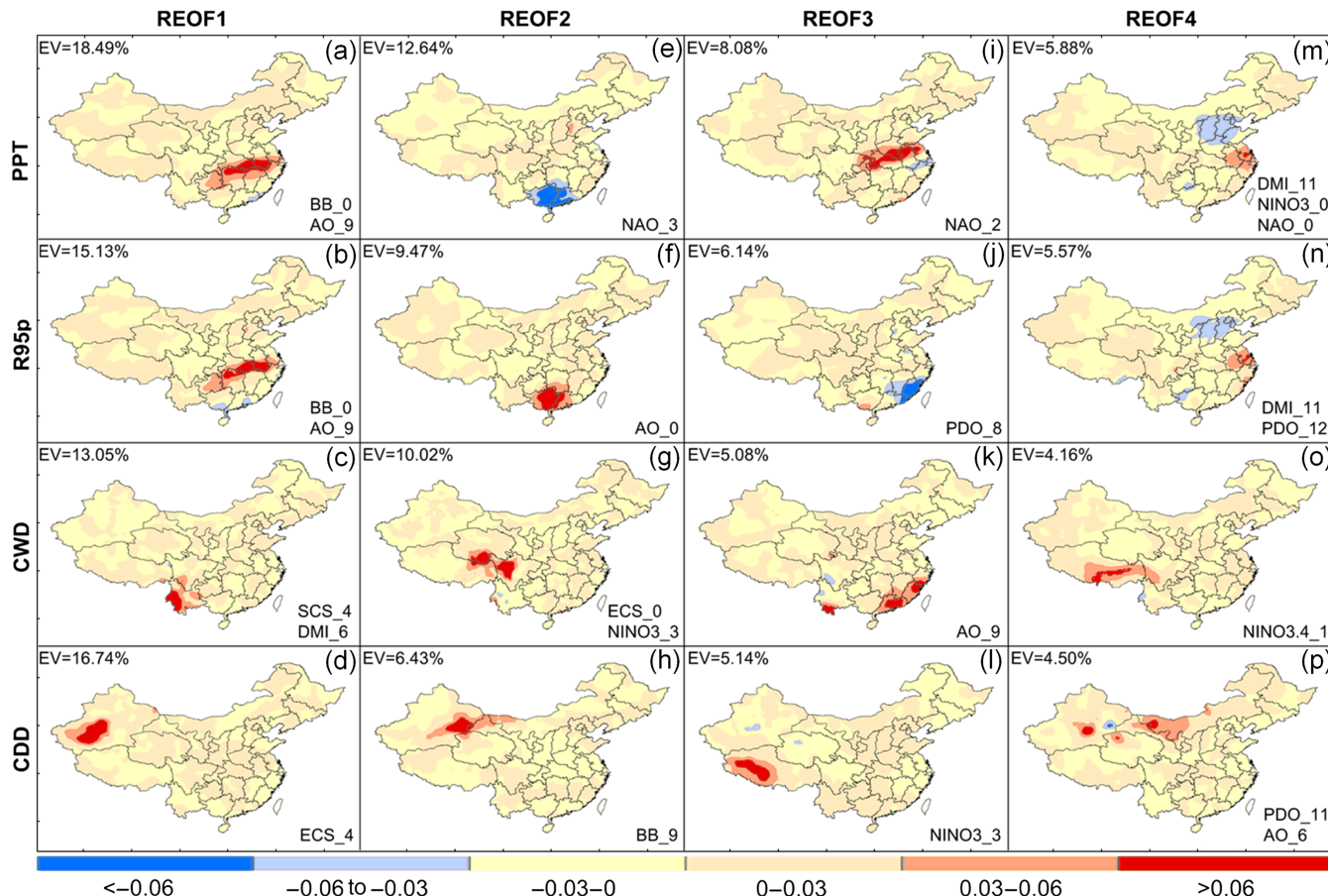


FIGURE 7 Spatial patterns of the leading four rotated EOFs for summer precipitation indices

**TABLE 6** As Table 4, but for summer

RPCs	Dominant influencing factors		$R^2$
PPT_RPC1	BB_0 (0.38)	AO_9 (-0.29)	23.88
PPT_RPC2	NAO_3 (0.32)		10.34
PPT_RPC3	NAO_2 (-0.33)		11.06
PPT_RPC4	DMI_11 (-0.45)	NINO3_0 (0.43)	35.31
		NAO_0 (-0.28)	
R95p_RPC1	BB_0 (0.35)	AO_9 (-0.32)	23.29
R95p_RPC2	AO_0 (0.28)		7.97
R95p_RPC3	PDO_8 (0.35)		12.23
R95p_RPC4	DMI_11 (-0.48)	PDO_12 (-0.29)	30.32
CWD_RPC1	SCS_4 (-0.39)	DMI_6 (0.30)	24.60
CWD_RPC2	ECS_0 (-0.38)	NINO3_3 (0.32)	24.13
CWD_RPC3	AO_9 (-0.30)		8.72
CWD_RPC4	NINO3.4_1 (-0.38)		14.27
CDD_RPC1	ECS_4 (-0.44)		19.27
CDD_RPC2	BB_9 (0.30)		9.09
CDD_RPC3	NINO3_3 (0.30)		8.71
CDD_RPC4	PDO_11 (-0.38)	AO_6 (-0.30)	26.15

#### 4.3.4 | Autumn

For autumn precipitation (see Figure 8 and Table 7), sensitive areas of the three wet indices are all observed in Guanzhong Basin and its surrounding areas (Figure 8a–c). Autumn accumulated precipitation in Guanzhong Basin tends to be increased by negative ECS\_7 and DMI\_9 (Figure 8a), and these two factors together explain 24% temporal changes in RPC1 of autumn PPT. The negative NINO3.4\_0, NINO3\_1 and ECS\_6 tend to increase autumn heavy precipitation in Guanzhong Basin and Hainan Province located in the southernmost part of China (Figure 8b), and 40% temporal changes in RPC1 of autumn R95p can be explained by these climate indices. BB shows most significant impacts on autumn CWD and CDD. The correlation coefficient between RPC1 of autumn CWD and BB\_0 is up to -0.67. The BB\_0, ECS\_8, NINO3.4\_4 and NINO3\_5 together explain 64% temporal variability for this mode. In addition, negative BB\_10, DMI\_0 and positive NAO\_9 tend to increase autumn CDD in the northern Tibet Plateau (Figure 8d), and 35% temporal variation in RPC1 of autumn CDD can be explained by these climate indices.

#### 4.4 | Assessment of explanation skill of identified climate indices

The couples (RPCs of seasonal precipitation indices vs. the corresponding dominant climate indices) with higher correlation coefficient (top 8) are plotted in Figure 9 as examples to examine the relationships between the rotated temporal signals of seasonal precipitation indices and the corresponding identified dominant climate indices. Similar fluctuation in the oscillatory patterns of each couple can be observed in all subfigures in Figure 9. It seems that the variability in the

temporal patterns of seasonal precipitation indices can be tracked to a great extent via identified climate indices. The question is whether the identified climate indices are helpful for forecasting seasonal extreme precipitation in China. To do this, the stepwise regression is performed over each of grid cells with the identified dominant climate indices from the first four RPCs for each of extreme precipitation indices (including PPT). Then the regression  $R^2$  of these dominant climate indices representing for their skill in explaining the inter-annual variability of each seasonal extreme precipitation index is calculated and then shown in Figure 10. In winter, the temporal variability of PPT (Figure 10a) and R95p (Figure 10b) over some grids located in south of Nanling Mountain can be explained up to more than 50% by the identified dominant influencing factors. We note that south of Nanling Mountain with higher  $R^2$  is just the sensitive area identified by the REOF1 of winter PPT (Figure 5a) and R95p (Figure 5b). For spring, the southeastern Hilly area is the sensitive area identified by REOF1 of spring PPT (Figure 6e) and R95p (Figure 6f), in where the identified climate indices have higher contribution in explaining inter-annual variability. Similarly, temporal variability of spring CWD (Figure 10g) can be better explained by the identified climate indices in the sensitive areas highlighted by the spatial patterns of its REOF2 (Figure 6g) and REOF4 (Figure 6o). Temporal variability of dry condition in spring can be better explained in the western area of Tarim Basin (Figure 10h) which is the sensitive area identified by REOF2 of spring CDD (Figure 6h). Summer precipitation extremes are most difficult to predict. In the sensitive areas identified by the first rotated modes of all summer precipitation indices (Figure 7i–l), the identified climate indices only explain 10–20% temporal variability in each precipitation index (Figure 10i–l). As for autumn, the temporal variability of R95p (Figure 10n) and CWD (Figure 10o) in the sensitive areas, respectively, identified by their REOF1 (Figure 8n,o) can be better explained by the respectively identified climate indices, too.

Our hypothesis is that the skill of the identified climate indices in explaining inter-annual variability for seasonal precipitation indices is dependent upon the cumulative explained variance of the leading four modes of precipitation indices. Thus, we plot the spatial average and maximum  $R^2$  over the whole China against the cumulative (top four) RPCs contribution to the total data variance of the corresponding extreme precipitation index in Figure 11. It can be seen from Figure 11a that, in general, the areal average cumulative percentage of inter-annual variability explained by the identified dominant climate indices increases with the increase of the cumulative explained variance by top four REOFs. Figure 11b shows that when the cumulative explained variance is greater than 40%, the maximum  $R^2$  can be higher than 45% and the highest  $R^2$  is up to 58% in this study. We note that the positive correlations shown in Figure 11a,b are

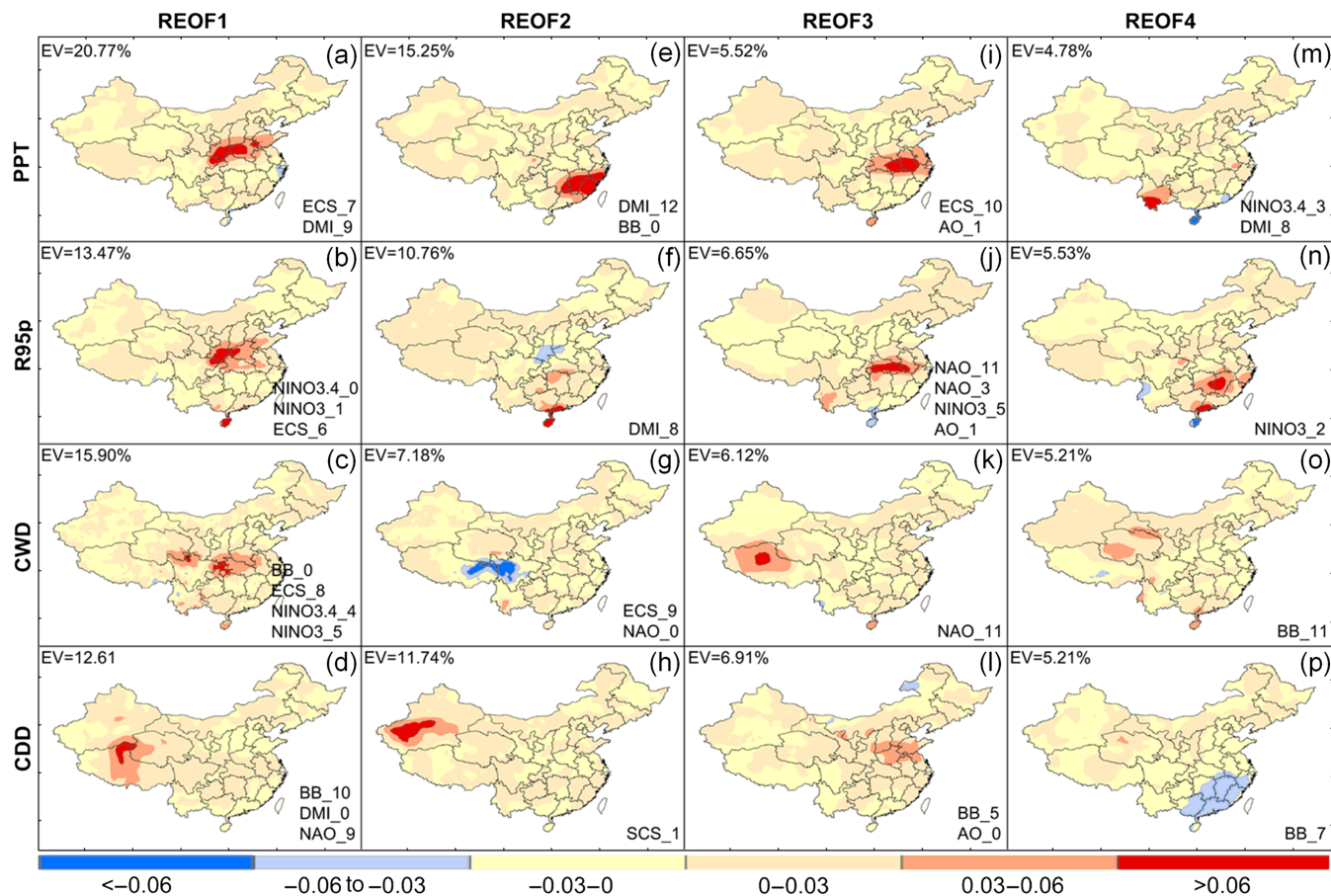


**FIGURE 8** Spatial patterns of the leading four rotated EOFs for autumn precipitation indices

**TABLE 7** As Table 4, but for autumn

RPCs	Dominant influencing factors			R <sup>2</sup>	
PPT_RPC1	ECS_7 (-0.38)	DMI_9 (-0.32)		24.00	
PPT_RPC2	DMI_12 (-0.31)	BB_0 (0.28)		19.25	
PPT_RPC3	ECS_10 (-0.32)	AO_1 (0.30)		22.08	
PPT_RPC4	NINO3.4_3 (0.46)	DMI_8 (-0.39)		31.59	
R95p_RPC1	NINO3.4_0 (-0.41)	NINO3_1 (-0.31)	ECS_6 (-0.28)	39.68	
R95p_RPC2	DMI_8 (0.28)			7.77	
R95p_RPC3	NAO_11 (0.43)	NAO_3 (0.36)	NINO3_5 (0.32)	AO_1 (0.28)	42.24
R95p_RPC4	NINO3_2 (0.28)				9.51
CWD_RPC1	BB_0 (-0.67)	ECS_8 (-0.57)	NINO3.4_4 (-0.31)	NINO3_5 (-0.30)	64.08
CWD_RPC2	ECS_9 (0.47)	NAO_0 (-0.37)			35.17
CWD_RPC3	NAO_11 (-0.28)				7.98
CWD_RPC4	BB_11 (0.28)				7.78
CDD_RPC1	BB_10 (-0.35)	DMI_0 (-0.33)	NAO_9 (0.31)		34.75
CDD_RPC2	SCS_1 (-0.36)				13.08
CDD_RPC3	BB_5 (0.53)	AO_0 (-0.32)			34.85
CDD_RPC4	BB_7 (-0.35)				12.43

statistically significant at 5% significance level. According to these results, we can conclude that the dominant influencing factors identified by REOFs combining with cross-correlation analysis and stepwise variable selection can be potential predictors for seasonal extreme precipitation to some extent.

## 5 | DISCUSSION

Compared with previous studies on the variability of extreme precipitation in China, this study gives a more comprehensive investigation on variability of both wet and dry conditions for extreme precipitation over China at seasonal

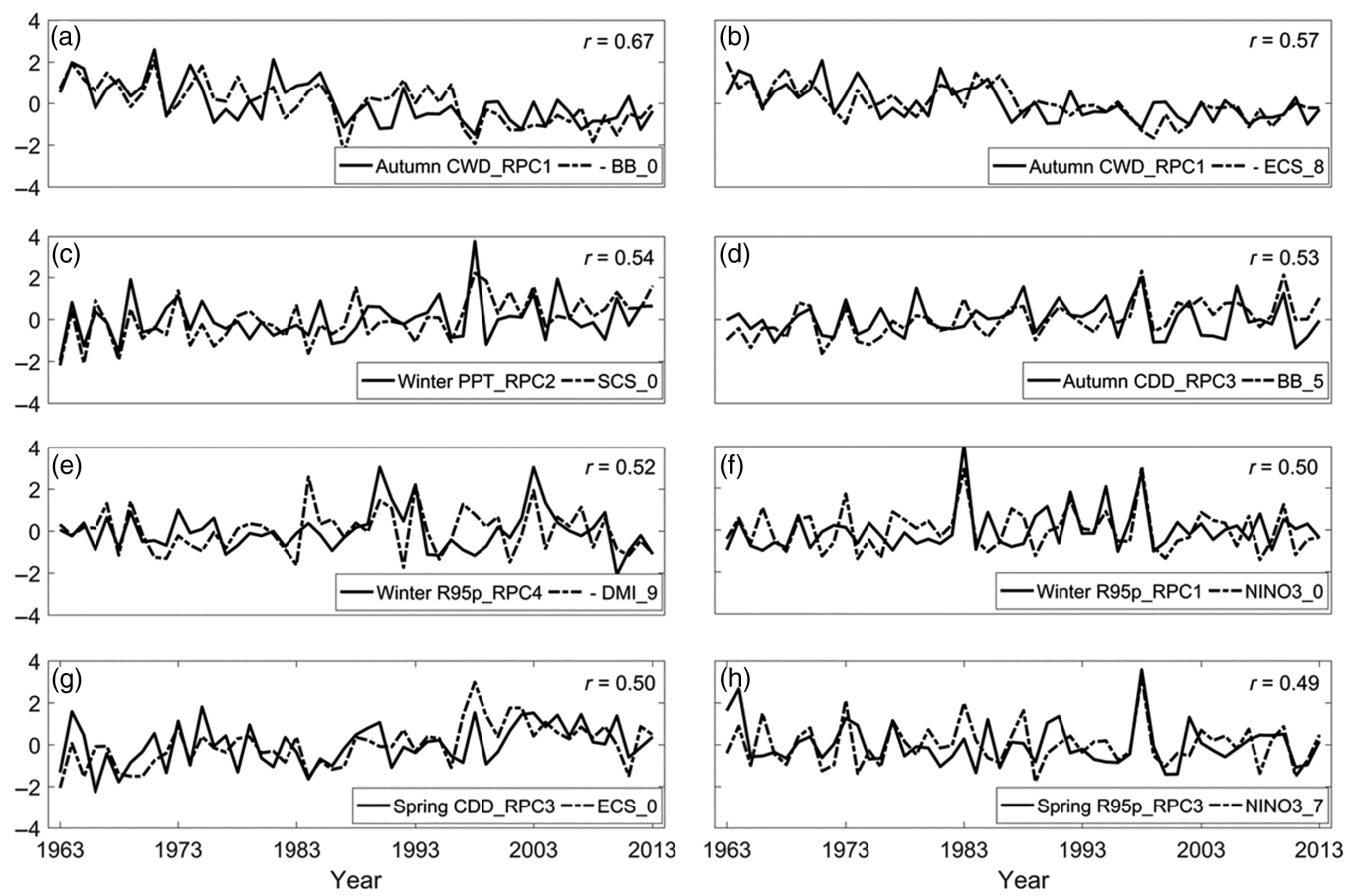


**FIGURE 9** Plots for RPCs of seasonal precipitation indices versus the corresponding dominant climate indices with higher correlation coefficient (top 8)

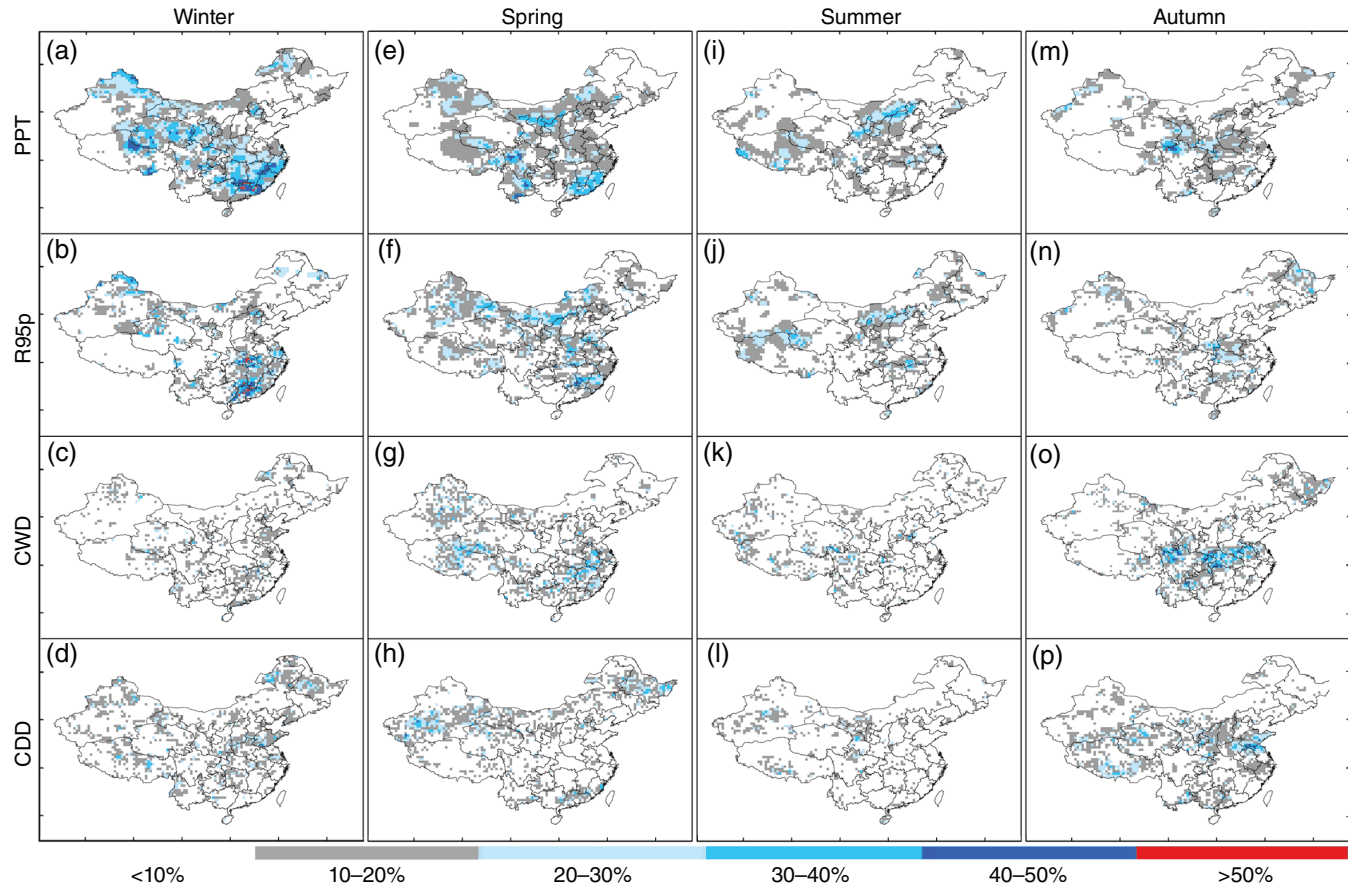


**FIGURE 10** Cumulative skill of the identified dominant influencing factors in explaining interannual variability of seasonal precipitation indices

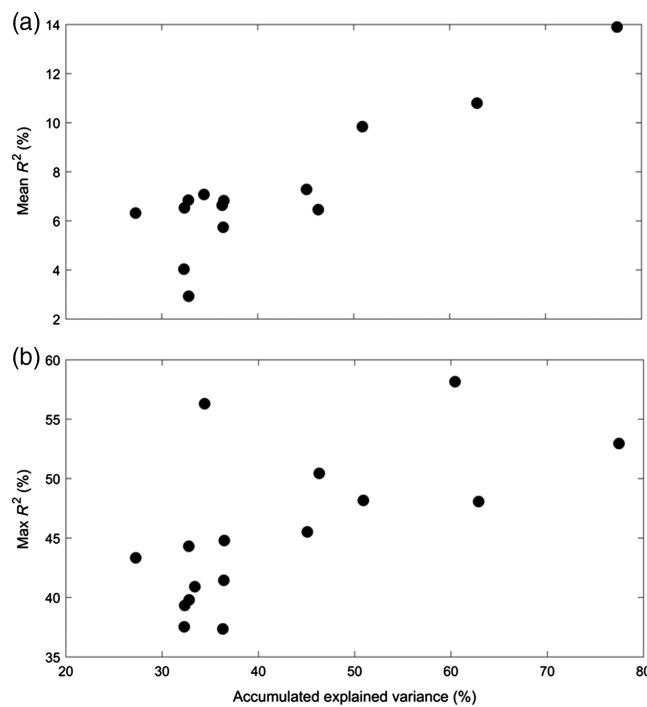


**FIGURE 11** Correlation between the areal average (a) and maximum (b) cumulative skill of identified influencing factors in explaining interannual variability of seasonal precipitation indices over China versus the cumulative explained variance of the leading four modes for corresponding precipitation index

scale, as well as their association with large-scale ocean–atmosphere oscillations. It provides more detailed information about extreme precipitation changes over China. The trend analysis results in this study are generally in accordance with previous studies (Zhai *et al.*, 2005; Wang and Yang, 2017) that extreme precipitation increased across all seasons in northwest China and decreased in the south and central area of China in spring and autumn. It should be noted that some inconsistencies are found too. For example, Wang and Yang (2017) concluded that wintertime extreme precipitation has increased persistently over the whole China; however, in this study some regions experienced a decreasing trend such as the southern part of Qinghai–Tibet region. This discrepancy may be caused by the difference of data types with different time period used in the two studies. The data set used in Wang and Yang (2017) was station data of 676 stations obtained from the National Meteorological Information Center, while in this study, the reanalysis daily precipitation data of 3,825 grids downloaded from the China Meteorological Data Sharing Service Network are used. Whether or not the grid data adopted in this study reveal more spatial patterns in the trends remain to be further investigated.

This is the first attempt that the REOFs method combining with lag correlation analysis and stepwise regression method is adopted to investigate the spatial patterns of seasonal extreme precipitation over China and their associations with large-scale ocean–atmosphere oscillations. Sensitive

areas of leading modes for each season can be found by using REOF method, and such results for four different seasons over the whole China is first given in this study. Sensitive areas of three spring wet indices are all located in southeastern areas of Southeast Hilly while those of summer PPT and R95p are both located in the middle and lower regions of Yangtze River basin, which may be related to the movement of the frontal rain band in China. The REOFs method coupling cross-correlation and stepwise variable selection appears to be effective in identifying the dominant influencing factors from the candidate climate indices. A part of our results has been shown by the consistent results with previous studies using different data set and methods. For example, we found that sensitive areas of winter wet precipitation indices are mostly observed in south of Nanling Mountain area where extreme precipitation is significantly influenced by ENSO events, which is consistent with the conclusion made by previous studies (Tao and Zhang, 1998; Wu *et al.*, 2003) that the variability of southern China winter precipitation was modulated by ENSO. In addition, we found that the BB\_0 has the most significant influences on summer PPT and R95p in the middle and lower reaches of Yangtze River basin excluding coastal area. A similar conclusion has been made by Bin *et al.* (2013) that the BB supplied strong moisture to the Yangtze River basin area in summer (July).

Precipitation in summer is plentiful, but the identified climate indices in this study appear to have relatively low skill in explaining the inter-annual variability of selected precipitation indices. This is likely because of the complexity of precipitation variation in this season. Besides, summer precipitation in China is influenced by other factors except for the climate indices mentioned in this study, including East Asian monsoon, Northwest Pacific subtropical high, Arctic sea ice, mainland snow cover, surface thermal status and solar activity.

In this study, the variability patterns of selected target precipitation indices over China are illustrated by REOF, and the first four RPCs are used to search the dominant large-scale climate indices. The RPCs, in contrast to each grid, reflect the spatial coherence of the temporal variability of precipitation index, and thus more likely contain the signals of large-scale teleconnection. The increasing skill for the case with a larger cumulative REOF contribution to the total temporal and spatial variance of the target variable is supportive evidence for this method. It should be noted that, this national-level analysis may bury some information from that based on subregions. Whether or not this loss of information reduces explanation capacity remains to be investigated in the future.

## 6 | CONCLUSIONS

In this study, we investigated the spatial distribution, trends and coherent spatial patterns of temporal variability of

seasonal precipitation extremes during 1963–2013 over China, and identified the dominant climate indices influencing regional extreme precipitation changes by analysing the statistical association between temporal patterns of three precipitation extreme indices and nine large-scale ocean–atmosphere indices with time lags of 0–12 months. Extreme wet conditions are remarkable in seasons except for winter in south and central China, and extreme dry events mostly occur in four seasons in northwest China. However, northwest China exhibits a wetting tendency in all seasons and south and central China a drying tendency in spring and autumn. The sensitive areas of two extreme wet indices highlighted by their REOFs are almost consistent with each other in the same season. These highlighted sensitive areas are mainly south of Nanling Mountain for winter, southern area of southeastern Hill for spring, mid-lower reaches of Yangtze River basin excluding coastal area for summer and Guanzhong Basin for autumn. The different spatial patterns of precipitation indices for each season show different linkages to the selected climate indices with different time lags. Moreover, the regional responses of precipitation extremes are complex when the identified climate indices are at different stages. The results show that the temporal changes of seasonal precipitation extremes can be partly explained by the identified dominant climate indices, and the explanations are very successful in their sensitive areas. It is worthy to mention that negative BB\_0, ECS\_8, NINO3.4\_4 and NINO3\_5 tend to increase autumn CWD in Guanzhong Basin and the intersection of Sichuan and Qinghai Province, and these four indices can together explain 64% temporal variability for the first rotated mode of autumn CWD. We emphasize that eight chosen couples of RPCs (of seasonal precipitation indices) and the identified climate indices exhibit very similar fluctuation with each other in their oscillatory patterns, indicating that the variability in the temporal patterns of seasonal precipitation extremes could be tracked to a great extent via the identified climate indices. Finally, the identified dominant climate indices were proved to be potential predictors for precipitation extremes especially in the identified sensitive areas, and can better explain the inter-annual variability of seasonal precipitation extremes for winter, spring and autumn than for summer. Moreover, precipitation indices related to precipitation amount can be better explained than those related to wet or dry spell. At the same time, the explanation skill of the identified climate indices largely depends on the cumulative explained variance of the leading four modes for corresponding seasonal precipitation index.

## ACKNOWLEDGEMENTS

We thank the anonymous reviewers for their carefully reading and constructive comments that improved the paper. This study was funded by the National Natural Science

Foundation of China (Grant Nos. 41472238 and 41571021), Construct Program of Key Discipline in Hunan Province of China (Grant No. 2011001) and Hunan Bairen Program (Grant No. 2012001). The data for the model used in this study are freely available at <http://www.cpc.ncep.noaa.gov> and <http://www.cdc.noaa.gov>.

## ORCID

Xinguang He  <http://orcid.org/0000-0002-7570-3224>

## REFERENCES

- Bin, C., Xiang, D.X. and Tianliang, Z. (2013) Main moisture sources affecting lower Yangtze River basin in boreal summers during 2004–2009. *International Journal of Climatology*, 33(4), 1035–1046. <https://doi.org/10.1002/joc.3495>.
- Casanueva Vicente, A., Rodríguez Puebla, C., Frías Domínguez, M.D. and González Reviriego, N. (2014) Variability of extreme precipitation over Europe and its relationships with teleconnection patterns. *Hydrology and Earth System Sciences*, 18(2), 709–725. <https://doi.org/10.5194/hess-18-709-2014>.
- Chen, W., Feng, J. and Wu, R. (2013) Roles of ENSO and PDO in the link of the East Asian winter monsoon to the following summer monsoon. *Journal of Climate*, 26(2), 622–635. <https://doi.org/10.1175/jcli-d-12-00021.1>.
- Chen, A.J., He, X.G., Guan, H.D. and Cai, Y. (2018) Trends and periodicity of daily temperature and precipitation extremes during 1960–2013 in Hunan Province, central South China. *Theoretical and Applied Climatology*, 132, 71–88. <https://doi.org/10.1007/s00704-017-2069-x>.
- Clow, D.W. (2010) Changes in the timing of snowmelt and streamflow in Colorado: a response to recent warming. *Journal of Climate*, 23(9), 2293–2306. <https://doi.org/10.1175/2009jcli2951.1>.
- Draper, N.R. and Smith, H. (1998) *Applied Regression Analysis*. Hoboken, NJ: Wiley Interscience.
- Fan, L., Lu, C., Yang, B. and Chen, Z. (2012) Long-term trends of precipitation in the North China Plain. *Journal of Geographical Sciences*, 22(6), 989–1001. <https://doi.org/10.1007/s11442-012-0978-2>.
- Fu, G.B., Yu, J.J., Yu, X.B., Ouyang, R.L., Zhang, Y.C., Wang, P., Liu, W.B. and Min, L.L. (2013) Temporal variation of extreme rainfall events in China, 1961–2009. *Journal of Hydrology*, 487, 48–59. <https://doi.org/10.1016/j.jhydrol.2013.02.021>.
- Gemmer, M., Fischer, T. and Jiang, T. (2011) Trends in precipitation extremes in the Zhujiang River basin, South China. *Journal of Climate*, 24, 750–761. <https://doi.org/10.1175/2010jcli3717.1>.
- Gershunov, A. and Barnett, T.P. (1998) ENSO influence on intraseasonal extreme rainfall and temperature frequencies in the contiguous United States: observations and model results. *Journal of Climate*, 11(7), 1575–1586. [https://doi.org/10.1175/1520-0442\(1998\)011<1575:eoier>2.0.CO;2](https://doi.org/10.1175/1520-0442(1998)011<1575:eoier>2.0.CO;2).
- Gong, D.Y. and Ho, C.H. (2003) Arctic Oscillation signals in the East Asian summer monsoon. *Journal of Geophysical Research*, 108, 2156–2202. <https://doi.org/10.1029/2002jd002193>.
- Grimm, A.M. and Saboia, J.P.J. (2015) Interdecadal variability of the South American precipitation in the monsoon season. *Journal of Climate*, 28(2), 755–775. <https://doi.org/10.1175/jcli-d-14-00046.1>.
- Grimm, A.M. and Tedeschi, R.G. (2009) ENSO and extreme rainfall events in South America. *Journal of Climate*, 22(7), 1589–1609. <https://doi.org/10.1175/2008jcli2429.1>.
- Gu, X.H., Zhang, Q., Singh, V.P. and Shi, P.J. (2017) Changes in magnitude and frequency of heavy precipitation across China and its potential links to summer temperature. *Journal of Hydrology*, 547, 718–731. <https://doi.org/10.1016/j.jhydrol.2017.02.041>.
- Hannachi, A., Jolliffe, I.T. and Stephenson, D.B. (2007) Empirical orthogonal functions and related techniques in atmospheric science: a review. *International Journal of Climatology*, 27(9), 1119–1152. <https://doi.org/10.1002/joc.1499>.
- Hartmann, H., Becker, S. and King, L. (2008) Predicting summer rainfall in the Yangtze River basin with neural networks. *International Journal of Climatology*, 28(7), 925–936. <https://doi.org/10.1002/joc.1588>.

- IPCC. (2012) *Managing the Risk of Extreme Events and Disasters to Advance Climate Change Adaptation. A Special Report of Working Groups I and II of the Intergovernmental Panel on Climate Change*. Cambridge and New York, NY: Cambridge University Press, 582 pp.
- Jiang, F., Hu, R.J., Wang, S.P., Zhang, Y.W. and Tong, L. (2013) Trends of precipitation extremes during 1960–2008 in Xinjiang, the northwest China. *Theoretical and Applied Climatology*, 111(1–2), 133–148. <https://doi.org/10.1007/s00704-012-0657-3>.
- Kendall, M.G. (1975) *Rank Correlation Methods*. Oxford: Griffin.
- Linderholm, H.W., Ou, T.H., Jeong, J.H., Folland, C.K., Gong, D.Y., Liu, H.B., Liu, Y. and Chen, D.L. (2011) Interannual teleconnections between the summer North Atlantic oscillation and the East Asian summer monsoon. *Journal of Geophysical Research*, 116, D13107. <https://doi.org/10.1029/2010jd015235>.
- Mann, H.B. (1945) Nonparametric tests against trend. *Econometrica: Journal of the Econometric Society*, 13(3), 245–259. <https://doi.org/10.2307/1907187>.
- North, G.R., Bell, T.L., Cahalan, R.F. and Moeng, F.J. (1982) Sampling errors in the estimation of empirical orthogonal functions. *Monthly Weather Review*, 110, 699–706. [https://doi.org/10.1175/1520-0493\(1982\)110<0699:seito>2.0.CO;2](https://doi.org/10.1175/1520-0493(1982)110<0699:seito>2.0.CO;2).
- Paredes Trejo, F., Brito-Castillo, L., Barbosa Alves, H. and Guevara, E. (2016) Main features of large-scale oceanic–atmospheric circulation related to strongest droughts during rainy season in Brazilian São Francisco River basin. *International Journal of Climatology*, 36, 4102–4117. <https://doi.org/10.1002/joc.4620>.
- Peng, Z., Wang, Q.J., Bennett, J.C., Pokhrel, P. and Wang, Z. (2014) Seasonal precipitation forecasts over China using monthly large-scale oceanic–atmospheric indices. *Journal of Hydrology*, 519, 792–802. <https://doi.org/10.1016/j.jhydrol.2014.08.012>.
- Peterson, T.C. (2005) The workshop on enhancing south and central Asian climate monitoring and indices. *CLIVAR Exchanges*, 10(2), 6.
- Peterson, T.C., Folland, C., Gruza, G., Hogg, W., Mokssit, A. and Plummer, N. (2001) *Report of the Activities of the Working Group on Climate Change Detection and Related Rapporteurs*. Geneva: World Meteorological Organization.
- Qin, D.H., Zhang, J.Y., Shan, C. and Song, L. (2015) *China National Assessment Report on Risk Management and Adaptation of Climate Extremes and Disasters*. Beijing: Science Press (in Chinese).
- Sillmann, J., Thorarinsdottir, T., Keenlyside, N., Schaller, N., Alexander, L.V., Hegerl, G., Seneviratne, S.I., Vautard, R., Zhang, X.B. and Zwiers, F.W. (2017) Understanding, modeling and predicting weather and climate extremes: challenges and opportunities. *Weather and Climate Extremes*, 18, 65–74. <https://doi.org/10.1016/j.wace.2017.10.003>.
- Tao, S.Y. and Zhang, Q. (1998) Response of the Asian winter and summer monsoon to ENSO events. *Scientia Atmosferica Sinica*, 22, 399–407 (in Chinese). <https://doi.org/10.3878/j.issn.1006-9895.1998.04.02>.
- Wang, F. and Yang, S. (2017) Regional characteristics of long-term changes in total and extreme precipitations over China and their links to atmospheric–oceanic features. *International Journal of Climatology*, 37(2), 751–769. <https://doi.org/10.1002/joc.4737>.
- Wang, W.G., Shao, Q.X., Yang, T.S., Peng, Z., Yu, Z.B., Taylor, J., Xing, W.Q., Zhao, C.P. and Sun, F.C. (2013) Changes in daily temperature and precipitation extremes in Yellow River basin, China. *Stochastic Environmental Research and Risk Assessment*, 27, 401–421. <https://doi.org/10.1007/s00477-012-0615-8>.
- Wang, F., Yang, S., Higgins, W., Li, Q. and Zuo, Z. (2014) Long-term changes in total and extreme precipitation over China and the United States and their links to oceanic–atmospheric features. *International Journal of Climatology*, 34, 286–302. <https://doi.org/10.1002/joc.3685>.
- Wu, R.G., Hu, Z.Z. and Kirtman, B.P. (2003) Evolution of ENSO related rainfall anomalies in East Asia. *Journal of Climate*, 16, 3742–3758. [https://doi.org/10.1175/1520-0442\(2003\)016<3742:eoerai>2.0.CO;2](https://doi.org/10.1175/1520-0442(2003)016<3742:eoerai>2.0.CO;2).
- Xiao, M., Zhang, Q. and Singh, V.P. (2015) Influences of ENSO, NAO, IOD and PDO on seasonal precipitation regimes in the Yangtze River basin, China. *International Journal of Climatology*, 35(12), 3556–3567. <https://doi.org/10.1002/joc.4228>.
- Xiao, M., Zhang, Q. and Singh, V.P. (2017) Spatiotemporal variations of extreme precipitation regimes during 1961–2010 and possible teleconnections with climate indices across China. *International Journal of Climatology*, 37(1), 468–479. <https://doi.org/10.1002/joc.4719>.
- Yang, L., Villarini, G., Smith, J.A., Tian, F. and Hu, H. (2013) Changes in seasonal maximum daily precipitation in China over the period 1961–2006. *International Journal of Climatology*, 33, 1646–1657. <https://doi.org/10.1002/joc.3539>.
- Ying, K., Frederiksen, C.S., Zhao, T.X., Zheng, G., Xiong, Z., Yi, X. and Li, C.X. (2018) Predictable and unpredictable modes of seasonal mean precipitation over northeast China. *Climate Dynamics*, 50, 3081–3095. <https://doi.org/10.1007/s00382-017-3795-6>.
- Yuan, Y., Yang, H., Zhou, W. and Li, C. (2008) Influences of the Indian Ocean Dipole on the Asian summer monsoon in the following year. *International Journal of Climatology*, 28(14), 1849–1859. <https://doi.org/10.1002/joc.1678>.
- Zhai, P., Zhang, X., Wan, H. and Pan, X. (2005) Trends in total precipitation and frequency of daily precipitation extremes over China. *Journal of Climate*, 18(7), 1096–1108. <https://doi.org/10.1175/jcli-3318.1>.
- Zhang, Q., Singh, V.P., Li, J., Jiang, F.Q. and Bai, Y.G. (2012) Spatio-temporal variations of precipitation extremes in Xinjiang, China. *Journal of Hydrology*, 434, 7–18. <https://doi.org/10.1016/j.jhydrol.2012.02.038>.
- Zilli, M.T., Carvalho, L.V. and Lintner, B.R. (2016) Decadal variability of the position and strength of the South Atlantic Convergence Zone and its relationship to precipitation variability and extremes over southeastern Brazil. *AGU Fall Meeting Abstracts*, A51C-0048.
- Zwiers, F.W., Alexander, L.V., Hegerl, G.C., Knutson, T.R., Kossin, J.P., Naveau, P., Nicholls, N., Schar, C., Seneviratne, S.I. and Zhang, X.B. (2013) Climate extremes: challenges in estimating and understanding recent changes in the frequency and intensity of extreme climate and weather events. In: *Climate Science for Serving Society*. Dordrecht: Springer, pp. 339–389. [https://doi.org/10.1007/978-94-007-6692-1\\_13](https://doi.org/10.1007/978-94-007-6692-1_13).

**How to cite this article:** Chen A, He X, Guan H, Zhang X. Variability of seasonal precipitation extremes over China and their associations with large-scale ocean–atmosphere oscillations. *Int J Climatol*. 2018;1–16. <https://doi.org/10.1002/joc.5830>